
Simulating Infinite-dimensional Nonlinear Diffusion Bridges

Gefan Yang¹ Elizabeth Louise Baker¹ Michael L. Severinsen²
 Christy Anna Hipsley³ Stefan Sommer¹

¹Department of Computer Science, University of Copenhagen

²Globe Institute, University of Copenhagen

³Department of Biology, University of Copenhagen

¹{gy,elba,sommer}@di.ku.dk

²michael.baand@sund.ku.dk

³christy.hipsley@bio.ku.dk

Abstract

The diffusion bridge is a type of diffusion process that conditions on hitting a specific state within a finite time period. It has broad applications in fields such as Bayesian inference, financial mathematics, control theory, and shape analysis. However, simulating the diffusion bridge for natural data can be challenging due to both the intractability of the drift term and continuous representations of the data. Although several methods are available to simulate finite-dimensional diffusion bridges, infinite-dimensional cases remain unresolved. In the paper, we present a solution to this problem by merging score-matching techniques with operator learning, enabling a direct approach to score-matching for the infinite-dimensional bridge. We construct the score to be discretization invariant, which is natural given the underlying spatially continuous process. We conduct a series of experiments, ranging from synthetic examples with closed-form solutions to the stochastic nonlinear evolution of real-world biological shape data, and our method demonstrates high efficacy, particularly due to its ability to adapt to any resolution without extra training.

1 Introduction

Diffusion processes are commonly utilized in diverse scientific fields, including mathematics, physics, evolutionary biology, and finance, to model stochastic dynamics. Updating the posterior of the model through conditioning on existing observed data is a crucial element of the process, and there are several methods to achieve this. For example, the Gaussian process regression can be used for finite-dimensional or infinite-dimensional linear models [Shi and Choi, 2011], and finite-dimensional Doob’s h -transform is designed for finite nonlinear processes [Rogers and Williams, 2000, Chapter 6]. On the other hand, many data types, such as images and sound signals, are naturally continuous and described by functions, and the stochasticity is also nonlinear. One approach is to discretize and represent them by vectors using finite-dimensional models. However, a more natural way is to work directly in the infinite-dimensional function space, performing only finite-dimensional projections during inference. This functional formulation offers resolution-invariant features, which are more memory-efficient and demonstrate greater generalization capacities. Simulating infinite-dimensional linear processes has been studied in some research [Franzese et al., 2024, Lim et al., 2023, Pidstrigach et al., 2023], while the extension to the conditioning of nonlinear processes remains an open question.

Interest in the study of linear diffusion processes has surged recently, largely driven by the advancements in diffusion generative models. In diffusion generative models, the data undergoes

perturbation through a forward unconditional linear diffusion process, resulting in noise that follows a simple distribution and is easy to sample. The sampled noise is then transformed back to the clean data through a reverse process, which is also linear and can be learned by the score-matching techniques [Hyvärinen and Dayan, 2005, Vincent, 2011]. Recently, the study of diffusion models using stochastic differential equations (SDEs) and their mathematical interpretations has gained significant attention [Song et al., 2020, Huang et al., 2021]. Based on the rich research on the time-reversed diffusion processes and the design of neural network approximation, we show that similar techniques can be applied to simulate the conditioning of nonlinear diffusion processes.

In order to condition an infinite-dimensional nonlinear diffusion process on function-valued observations, we use the theory of infinite-dimensional Doob’s h -transform, as outlined in Baker et al. [2024]. This transformation converts an unconditional SDE into a conditional one, which is commonly referred to as the diffusion bridge [Delyon and Hu, 2006, Schauer et al., 2017, Heng et al., 2021]. Theoretically, the existence of such conditional processes has been established, and our research has focused on developing a numerically efficient method for their simulation. This involved reversing the time of the diffusion bridge, which adheres to an SDE characterized by a learnable drift. We also propose a tractable loss function for learning such drift, which is inspired by the denoising score-matching object [Vincent, 2011]. By directly tackling the learning of the infinite-dimensional process, we employ a time-dependent neural operator as the approximator. Given the temporal symmetry between the diffusion bridge and its reversal, we simulate the reversed bridge backward in time, effectively recreating paths of the original bridge and thereby resolving the issue.

We aim to incorporate the score-matching techniques into the diffusion bridge simulation methodology, especially to handle infinite-dimensional nonlinear bridges. Our contributions are outlined as follows:

- Our study introduces a novel approach for simulating infinite-dimensional nonlinear diffusion bridges utilizing a score-matching technique. Expanding upon the research of [Heng et al., 2021] that concentrated on simulating bridges in finite dimensions, we further develop this technique to encompass infinite dimensions. By directly approximating the additional drift introduced by the infinite-dimensional Doob’s h -transform, we are able to reverse the diffusion bridge and simulate it backward using the learned drift operator. This framework holds the potential for addressing simulating general infinite-dimensional nonlinear diffusion bridges, especially those that involve continuous data within infinite-dimensional function spaces.
- In order to approximate the drift operator in the reversed bridge, we have devised a continuous time-dependent neural operator architecture that draws inspiration from the Fourier time modulation [Park et al., 2023] and the U-shaped neural operator [Ashiqur Rahman et al., 2022]. This structure is able to represent continuous time-dependent nonlinear operators that are shown to be discretization invariant. Furthermore, by splitting the large nonlinear transition step into small tractable Gaussian steps, we design the loss function on the Gaussian steps and, therefore, holds a computable form.
- We illustrate our proposed methodology using continuous function-data-valued stochastic processes. This will involve a demonstration of the Brownian bridge with a closed-form drift, as well as the simulation of stochastic nonlinear biological shape evolution. To our best knowledge, this is the first time the nonlinear diffusion shape bridges can be simulated using a discretization-invariant framework.

2 Related work

Bridge simulations: The linear diffusion process always has a Gaussian transition density, which gives the additional drift term in the corresponding conditional process a closed form. The challenge

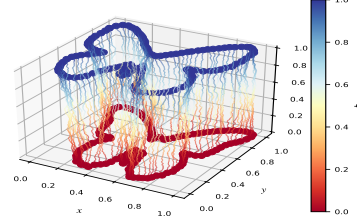


Figure 1: The nonlinear stochastic bridge between two continuous butterfly shapes (blue and red) is characterized by discrete landmarks. The nonlinearity of the bridge prevents the shape from overlapping and the landmarks from colliding, which could happen with a linear process.

lies in the nonlinear case, where the transition is no longer Gaussian. Several methods have been developed [Delyon and Hu, 2006, Van der Meulen and Schauer, 2020, Corstanje et al., 2024] for simulating bridges in different scenarios. The essential idea is to approximate the unknown drift with a proposed known one. The bridge, including such an approximate drift, is called the proposed process. By sampling from the proposed process and computing the likelihood ratio between the proposed and the true ones, the MCMC is used to correct the sampling. Such methods suffer from expensive matrix inversion in high-dimensional cases and time-costly MCMC updating iterations. Another approach is to directly approximate the drift, which is proposed by [Heng et al., 2021], where they use denoising score matching to learn the score for the finite-dimensional nonlinear bridge. Based on [Heng et al., 2021]’s work, we further generalize it to the infinite-dimensional settings.

Infinite-dimensional diffusion models: (Score-based) diffusion generative models (SGMs) are initially developed to generative samples in Euclidean spaces [Sohl-Dickstein et al., 2015, Song and Ermon, 2019, Song et al., 2021]. Various studies have been done to generalize SGMs into infinite-dimensional space with either Hilbert-space-defined score functions [Pidstrigach et al., 2023, Baldassari et al., 2024, Lim et al., 2023] or finite-dimensional score projections [Franzese et al., 2024, Hagemann et al., 2023]. However, due to the generative purpose, their methods are all limited to the linear SDEs (often referred to as variance preserving/exploring SDEs), i.e., with a diffusion term independent of the value of the process, and such SDEs are unconditional to the end states. While we consider a more general conditional nonlinear case, where the drift and diffusion terms are more complex to derive a closed-form solution.

Diffusion Schrödinger bridge: Another diffusion bridge related model is the diffusion Schrödinger bridge [De Bortoli et al., 2021, Shi et al., 2024, Tang et al., 2024, Thornton et al., 2022], where the transition between two distributions are treated as the optimal transport (OT) problem. Among them, the work in [Shi et al., 2024] is closely related to ours, as they also minimize the KL divergence to match the unknown bridge. However, since their focus is on generative purposes, a simpler finite-dimensional linear process and the bridge points are considered. We are instead interested in the imputation between the points.

3 Infinite-dimensional nonlinear bridges

3.1 Conditioning via infinite-dimensional Doob’s h -transform

The infinite-dimensional diffusion bridge can be achieved by applying the infinite-dimensional Doob’s h -transform [Baker et al., 2024] on an unconditional diffusion process. Let $(H, \langle \cdot, \cdot \rangle)$ denote a separable Hilbert space with a chosen countable orthonormal base $\{e_i\}_{i=1}^\infty$, and let $(\Omega, \mathcal{F}, \mathbb{P})$ be a probability space with natural filtration $\{\mathcal{F}_t\}$, let $\mathcal{B}(H)$ the Borel algebra, $\mathbb{P}(H)$ be the set of probability measures on $(H, \mathcal{B}(H))$ and μ_0, μ_T be two measures in $\mathbb{P}(H)$ that we want to bridge between. A H -valued diffusion process $X = (X(t))_{t \in [0, T]}$ is defined as:

$$dX(t) = f(t, X(t)) dt + g(t, X(t)) dW(t), \quad X_0 \sim \mu_0 \quad (1)$$

where $W(t)$ is a Wiener process in another Hilbert space U (where U can equal H) with a trace-class covariance operator C (i.e., $\text{Tr}(C) < \infty$), $f : [0, T] \times H \rightarrow H$, $g : [0, T] \times H \rightarrow \text{HS}(C^{1/2}(U), H)$, where $\text{HS}(C^{1/2}(U), H)$ denotes the Hilbert-Schmidt operator from $C^{1/2}(U)$ to H . We can then condition (1) on hitting $X(T) \sim \mu_T$ within a finite time T by applying infinite-dimensional Doob’s h -transform, such transformed diffusion process $X^c = (X^c(t))_{t \in [0, T]}$ follows the SDE:

$$dX^c(t) = \{f(t, X^c(t)) + a(t, X^c(t)) \nabla \log h(t, X^c(t))\} dt + g(t, X^c(t)) dW(t) \quad (2)$$

with $X^c(0) = x_0 \sim \mu_0$, $X^c(T) = x_T \sim \mu_T$, where $a := gg^* : [0, T] \times H \rightarrow \text{HS}(C^{1/2}(U), H)$, $\nabla \log h : [0, T] \times H \rightarrow C^{1/2}(U)$ is another Hilbert-Schmidt operator, we shall call it “score operator” for short in the following text. $h : [0, T] \times H \rightarrow H$ is the Doob’s h function, defined as $h(t, x) := \mathbb{P}(X(T) \sim \mu_T \mid X(t) = x)$. The composition $a(\cdot, \cdot) \nabla \log h(\cdot, \cdot) : [0, T] \times H \rightarrow H$ is then an operator that maps within H and, therefore, can be treated as the additional drift term.

In finite dimension, the $h : [0, T] \times \mathbb{R}^d \rightarrow (0, \infty)$ can be chosen as a function satisfying $h(t, x) = \int h(t+s, y) p_{(t+s)|t}(y \mid x) dy$ [Rogers and Williams, 2000, Chapter 6], where $p_{(t+s)|t}(y \mid x)$ is the conditional probability density with respect to the Lebesgue measure dy in \mathbb{R}^d . A common choice of h is $h(t, x) := p_{T|t}(y \mid x) / p_{T|0}(y \mid x_0)$, and therefore the score becomes $\nabla \log p_{T|0}(y \mid x_0)$. However, since the Lebesgue measure dy and the probability density p are no longer well-defined in

H , such a choice is unavailable for infinite dimension. The definition of $\nabla \log h$ as an operator, as described above, can be used to address the well-posedness of the score. However, simulating (2) is still nontrivial even with the finite-dimensional projection as used in [Franzese et al., 2024] because of the intractable conditional probability, which only has a closed form when g is X -independent. To simulate a more general nonlinear bridge, inspired by [Heng et al., 2021], we apply the generalized time reversal theorem on the bridge process, and it turns out that in the time-reversed bridge process, the additional drift term can be approximated by sampling from the unconditional process (1). In the following sections, we shall detail the infinite-dimensional time reversal and a learnable object.

3.2 Time-reversed bridges

Under specific conditions, the finite-dimensional version of (1) $X^d(t) \in \mathbb{R}^d$ has a time-reversed process $Y^d(t) \in \mathbb{R}^d$ that satisfies [Haußmann and Pardoux, 1986]:

$$\text{forward: } dX^d(t) = f^d(t, X^d(t)) dt + g^d(t, X^d(t)) dW^d(t), \quad X^d(t) \in \mathbb{R}^d, \quad (3)$$

$$\text{reversed: } dY^d(t) = \bar{f}^d(t, Y^d(t)) dt + g^d(T-t, Y^d(t)) dB^d(t), \quad Y^d(t) \in \mathbb{R}^d, \quad (4)$$

with $f^d : [0, T] \times \mathbb{R}^d \rightarrow \mathbb{R}^d$, $g^d : [0, T] \times \mathbb{R}^d \rightarrow \mathbb{R}^l$ as finite-dimensional drift and diffusion terms, $W^l(t)$, $B^l(t)$ are Wiener processes in \mathbb{R}^l , $\bar{f}^d(t, x) = -f^d(T-t, x) + \frac{1}{p_{T-t}(x)} \nabla[a^d(T-t, x)p_{T-t}(x)]$, and $p_t(x)$ as the probability density in \mathbb{R}^d . Furthermore, [Millet et al., 1989] shows that such a time reversal exists for infinite-dimensional SDEs. Suppose the Hilbert space U , where the Wiener process $W(t)$ lives, has a countable orthonormal basis $\{k_j\}_{j=1}^\infty$, with the basis $\{e_i\}_{i=1}^\infty$ of H , we can write (1) in terms of these bases:

$$dX_i(t) = f_i(t, X(t)) dt + \sum_j g_{ij}(t, X(t)) dW_j(t), \quad i = 1, \dots, \infty, \quad (5)$$

where $f_i : [0, T] \times H \rightarrow \mathbb{R}$ is defined as $\langle f(t, x), e_i \rangle$ and $g_{i,j} : [0, T] \times H \rightarrow \mathbb{R}$ is defined by $\langle g(t, x)(e_j), e_i \rangle$.

This has a family of time-reversed processes:

$$dY_i(t) = \bar{f}_i(T-t, Y(t)) dt + \sum_j g_{ij}(T-t, Y(t)) dB_j(t), \quad i = 1, \dots, \infty, \quad (6)$$

where $\bar{f}_i(t, x) = -f_i(t, x) + \frac{1}{p_{T-t}(x_i|\xi_i)} \sum_{j \in I(i)} \nabla_j[a_{ij}(T-t, x)p_{T-t}(x_i|\xi_i)]$, where $p_t(x_i|\xi_i)$ is the conditional probability density of $X^i(t) = (X_j(t), j \in I(i))$ given $(X_j(t), j \notin I(i)) = \xi_i$, and $I(i)$ is a finite set of indices characterized by i . Such a density is assumed to exist with respect to the Lebesgue measure in \mathbb{R}^I (See [Millet et al., 1989, Section 5]), which is a finite subspace of H . We can apply this time reversal upon the infinite-dimensional bridge (2) derived in the previous section and obtain the infinite-dimensional time-reversed bridge. We shall see that within this reversed bridge, the additional term does not require the information of μ_T , which makes it possible to learn from the process that starts from μ_0 without hitting μ_T .

Theorem 3.1. *Let f, g , and a be as defined before, and let $B(t)$ be a Wiener process in U . The conditional process $X^c(t)$ has a time-reversal $Y^c = (Y^c(t))_{t \in [0, T]} := X^c(T-t)$ following the SDE:*

$$dY^c(t) = \bar{f}(t, Y^c(t)) dt + g(T-t, Y^c(t)) dB(t) \quad (7)$$

where $\bar{f}(t, x) = -f(T-t, x) + a(T-t, x) \nabla \log \bar{h}(T-t, x) + \nabla \cdot a(t, x)$, and $\bar{h}(t, x) = \mathbb{P}(X(t) \in dx | X(0) = x_0) =: P(0, x_0, t, dx)$, which is the law of $X(t)$ given $X(0) = x_0$, and $\nabla \cdot a(t, x) := \sum_j \nabla_j a_{ij}(t, x)$.

The proof of Theorem 3.1 can be found in A.1. Note that (7) does not require μ_T . If the process starts from μ_0 , it is impossible to sample from μ_T conditioned on the intermediate distribution μ_t without constructing the bridge forehead. Therefore the h in (2) is actually inaccessible. In contrast, sampling from μ_t while conditioning on μ_0 is feasible, which can be achieved by sampling the unconditional process that starts from μ_0 . This insight makes learning \bar{h} possible instead. However, the general transition from 0 to t is still intractable unless the original process has an X -independent diffusion term, and then the transition shall be Gaussian, but we can address this issue by using the Markovian property of the process, which enable us to split the large transition into small steps with Gaussian-like transitions.

4 Learning the bridge

4.1 Learning the nonlinear drift

The idea of learning (7) is to minimize the distance between the estimated bridge and the true bridge in the sense of KL divergence, which is sometimes referred to as “bridge matching” [Shi et al., 2024, Liu et al., 2023a, Delbracio and Milanfar, 2023]. We can write the object function as the KL divergence between the estimated and the true bridge. However, the true bridge still has no closed form, and the object function is thereby uncomputable. Fortunately, the bridge is Markovian, which means any single transition step is independent of the history, or we can say the whole information of the process is “compressed” into a single small step. This property enables us to learn with only small local steps and average it over the whole trajectory to gain global information on the whole process.

Let \mathbb{P}^{x_0} denote the path measure induced by (7) starting from $Y^c(T) = x_0$, and $\mathbb{Q}_\theta^{x_0}$ be the path measure induced by another time-reversed process $Y = (Y(t))_{t \in [0, T]}$ follows:

$$dY(t) = f_\theta(t, Y(t)) dt + g(T - t, Y(t)) dB_t \quad (8)$$

where $f_\theta(t, x) = -f(T - t, x) + \mathcal{G}_\theta(T - t, x) + \nabla \cdot a(T - t, x)$, $\mathcal{G}_\theta : [0, T] \times H \rightarrow H$ is a parameterized operator by θ . Let $d\mathbb{P}^{x_0} / d\mathbb{Q}_\theta^{x_0}$ denote the Radon-Nikodym derivative of \mathbb{P}^{x_0} with respect to $\mathbb{Q}_\theta^{x_0}$, then by minimizing the KL divergence $D_{KL}(\mathbb{P}^{x_0} \mid \mathbb{Q}_\theta^{x_0}) = \mathbb{E}_{X(t)}[\log d\mathbb{P}^{x_0} / d\mathbb{Q}_\theta^{x_0}(X(t))]$, we shall approximate the bridge (7) using \mathcal{G}_θ .

Theorem 4.1. *For any time partition $(t_i)_{i=1}^n$ of the interval $[0, T]$, the loss function which is defined as:*

$$\hat{L}(\theta) := \frac{1}{2} \sum_{i=1}^n \int_{t_{i-1}}^{t_i} \mathbb{E}_{X(t)} [\|A_t(x) \{ \mathcal{G}_\theta(t, x) - b(t, x, t_{i-1}, x_{t_{i-1}}) \} \|_{U_0}] dt \quad (9)$$

is equivalent to $D_{KL}(\mathbb{P}^{x_0} \mid \mathbb{Q}_\theta^{x_0})$ up to a θ -independent C , where $b(t, x, t_{i-1}, x_{t_{i-1}}) := a(t, x_t) \nabla \log \mathbb{P}^{x_0}(X(t) \in dx \mid X(t_{i-1}) = x_{t_{i-1}})$, $A_t(x) = C^{-1/2} g^{-1}(t, x) : [0, T] \times H \rightarrow U$ is a θ -independent operator, $\| \cdot \|_U$ is the norm of U .

Furthermore, $A_t(x)$ is positive-definite because g and C are assumed to be positive, so $\ker(A_t(x)) = \{0\}$, and we can drop it when using gradient descent as suggested in [Lim et al., 2023]. Finally, we train with the following object function:

$$L(\theta) := \frac{1}{2} \sum_{i=1}^n \int_{t_{i-1}}^{t_i} \mathbb{E}_{X(t)} \{ \| \mathcal{G}_\theta(t, x) - b(t, x, t_{i-1}, x_{t_{i-1}}) \|_U^2 \} dt. \quad (10)$$

4.2 Time-dependent neural operators

As described in the previous section, $\mathcal{G}_\theta : [0, T] \times H \rightarrow H$ is a time-dependent operator. We use a time-dependent neural operator to approximate it. Neural operators are initially developed to solve partial differential equations where the mapping from initial conditions to solutions is treated as a nonlinear smooth operator [Li et al., 2020a,b, Lu et al., 2021, Kovachki et al., 2023]. Such a learned operator is shown to be independent of the mesh or discretization used during the training [Kovachki et al., 2023], thereby enabling them to operate on the continuous domain. We choose the Fourier neural operator (FNO) proposed in [Li et al., 2020a] for two main reasons: 1) FNO is efficient due to the Fast Fourier Transform (FFT) and easy to implement; 2) Within the FNO, the functions are decomposed by the Fourier basis, which can represent the continuous periodic signals. It is especially suitable for our use since we model closed shapes that can be treated as periodic.

Since our target operator \mathcal{G}_θ is time-dependent, we incorporate the time information by using the continuous-in-time FNO (CTFNO) proposed by [Park et al., 2023], which modulates the time embedding into the Fourier modes. Besides the time step modulation, we also refer to the design of UNO [Ashiqur Rahman et al., 2022], which is shown to outperform the classical FNO structure used in [Li et al., 2020a] with less memory and higher accuracy. By combining both, we propose the structure of U-shaped CTFNO, as shown in Figure 2. In practice, we first specify the discrete spatial-temporal grid on which the functions are evaluated. Normally, the grid resolution for training is lower than that for inference. We assume for both input and output functions, the dimension of the domains is 1, and the codomains are d_u and d_v , respectively. Then, the function evaluated at

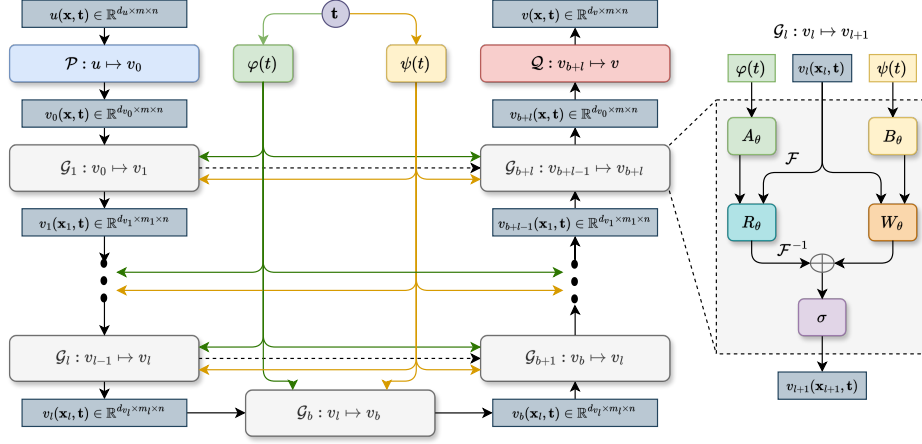


Figure 2: Continuous-time U-shaped FNO architecture, acting as a parameterized operator $\mathcal{G}_\theta : (u, t) \mapsto v$, where both u and v are evaluated on a discretized spatial-temporal grid (\mathbf{x}, \mathbf{t}) with $\mathbf{x} \in \mathbb{R}^m, \mathbf{t} \in \mathbb{R}^n$

m -discretized domains can be represented with the $m \times d_u$ matrix. In fact, in the context of bridge approximation, $d_u = d_v$, we keep the notation for generality. After discretizing the spatial-temporal grid as an $\mathbb{R}^m \times \mathbb{R}^n$ space, we evaluate u and obtain a finite-dimensional vector $u(\mathbf{x}, \mathbf{t}) \in \mathbb{R}^{d_u \times m \times n}$. Then $u(\mathbf{x}, \mathbf{t})$ and \mathbf{t} are fed into the neural operator. Within the operator, \mathcal{P} and \mathcal{Q} are lifting and projecting maps individually; the former increases the dimension of the codomain, and the latter decreases. Both these two projections are implemented as convolutional layers with 1-size kernels. At the same time, the time \mathbf{t} is transformed into two embeddings through φ and ψ . We implemented both as sinusoidal embeddings [Vaswani et al., 2017] as suggested in [Park et al., 2023]. The lifted $v_0(\mathbf{x}, \mathbf{t})$ and the embeddings $\varphi(t), \psi(t)$ are fed into one of the continuous-time Fourier layers \mathcal{G}_l . Within the block, the input v_0 is transformed into the Fourier modes through the FFT; Meanwhile, the embedding $\varphi(t)$ is transformed by a learnable linear transformation A_θ and will be used with a learnable linear transformation R_θ on the Fourier modes through $A_\theta \varphi(t) R_\theta \mathcal{F}(v_0)$. Conversely, $\psi(t)$ and v_0 shall go through a similar process, except all the actions are executed on the physical domain without Fourier transformation. Note that the output spatial dimension does not have to be equal to the input, i.e., $\mathbf{x}_{\text{out}} \in \mathbb{R}^{m_{\text{out}}}, \mathbf{x}_{\text{in}} \in \mathbb{R}^{m_{\text{in}}}, m_{\text{out}} \neq m_{\text{in}}$; that is, a spatial subspace is focused, which is similar to the classical U-net. Finally, the transformed Fourier component $\mathcal{F}^{-1}[A_\theta \varphi(t) R_\theta \mathcal{F}(v_0)]$ and the residual component $B_\theta \psi(t) W_\theta v_0$ are added and then activated by a point-wise nonlinear activation function σ . Mimic the traditional U-net, our neural operator is equipped with a decreasing hierarchy from top to bottom in two aspects: 1) the output spatial dimension is decreasing; 2) the truncated Fourier modes in FFT are decreasing. Both the designs are for extracting multi-level Fourier features [Ashiqur Rahman et al., 2022]. The skip connections between the downsampling and upsampling paths are kept as well. Compared to a normal FNO, our modified neural operator can achieve better performance with fewer parameters and fast convergence speed, thereby being suitable for the operator approximator in our case.

4.3 Numerical implementations

As we represent \mathcal{G}_θ as a neural operator, we implicitly project the infinite-dimensional optimization object 10 into finite dimension. Such projection $P^d : H \rightarrow \mathbb{R}^d$ can be achieved by, for example, taking the first d components $\{e_i\}_{i=1}^d \subset \{e_i\}_{i=1}^\infty$, and projecting the element $h \in H$ by $h^d = \sum_{i=1}^d \langle h, e_i \rangle_H \cdot e_i$. In the subspace $\mathbb{R}^d \subset H$, the conditional probability $\mathbb{P}(X(t) | X(0))$ has a density function $p(X^d(t) | X^d(0))$ given the defined Lebesgue measure. $X^d(t) \in \mathbb{R}^d$ is a finite-dimensional vector obtained by evaluating $X(t)$ on a finite-dimensional grid. To sample $X^d(t)$, we need to solve the finite-dimensional version of (1):

$$dX^d(t) = f^d(t, X^d(t)) dt + g^d(t, X^d(t)) dW^k(t), \quad X^d(0) \sim \mu_0^d, \quad (11)$$

where $f^d : [0, T] \times \mathbb{R}^d \rightarrow \mathbb{R}^d$, $g^d : [0, T] \times \mathbb{R}^d \rightarrow \mathbb{R}^{d \times k}$, W^k is a standard Wiener process lives in \mathbb{R}^k , μ_0^d is the push-forwards of μ_0 by the projection map $P^d : H \rightarrow \mathbb{R}^d$ Pidstrigach et al. [2023], defined by:

$$\mu^d := (P^d)_* \mu, \quad \text{where} \quad (P^d)_* \mu(A) = \mu((P^d)^{-1}(A)), A \subset H. \quad (12)$$

Solving (11) can be done using many finite-dimensional SDE numerical solving approaches. We choose the Euler-Maruyama solver (See, for example, [Bayram et al., 2018]). In the Euler-Maruyama scheme, the small-step transition is modeled as a Gaussian density, and the time integral from t_{i-1} to t_i can be approximated by the discrete sum. The single-step update of Euler-Maruyama is:

$$X^d(t_i) = X^d(t_{i-1}) + f^d(t_{i-1}, X^d(t_{i-1}))\delta t + g^d(t_{i-1}, X^d(t_{i-1}))(W^k(t_i) - W^k(t_{i-1})), \quad (13)$$

where $W^k(t_i) - W^k(t_{i-1}) \sim \mathcal{N}(0, \delta t I_k)$ is the independent Brownian increment. Then the approximate loss is:

$$L^d(\theta) := \frac{1}{2} \delta t \sum_{i=1}^n \mathbb{E}_{x_0} \{ \|\mathcal{G}_\theta(t_i, X^d(t_i)) - b^d(t_i, X^d(t_i), t_{i-1}, X^d(t_{i-1}))\|^2 \}. \quad (14)$$

As $\delta t \rightarrow 0$, $L^d(\theta) \rightarrow L(\theta)$ by the property of Euler-Maruyama solver. In practice, we choose the time steps as 0.01 within the total time interval $[0, 1]$, which we consider as a proper choice of balance between accuracy and efficiency. $b^d(t_i, X^d(t_i), t_{i-1}, X^d(t_{i-1})) = \Sigma^d(t_{i-1}, X^d(t_{i-1})) \cdot \nabla \log p(X^d(t_i) | X^d(t_{i-1}))$. Since p is Gaussian, $b^d(t_i, X^d(t_i), t_{i-1}, X^d(t_{i-1}))$ can be easily computed as:

$$b^d(t_i, X^d(t_i), t_{i-1}, X^d(t_{i-1})) = -\frac{1}{\delta t} \{X^d(t_i) - X^d(t_{i-1}) - \delta t f^d(t_{i-1}, X^d(t_{i-1}))\}. \quad (15)$$

Note that b^d can be computed simultaneously as the SDE-solving step iterates without additional computations afterward. So far, the parameterized operator \mathcal{G}_θ and the computable loss function $L^d(\theta)$ have been introduced. We summarize the algorithms for training and inference as Algorithm 1 and 2 in the Appendix.

5 Experiments

5.1 Functional Brownian bridges

Quadratic functions: We first study the function-valued Brownian process, whose score has a closed form when projected into the finite dimension. For the object functions, we choose the quadratic function $f(x) = ax^2 + \varepsilon$, where $a = \{1, -1\}$ and $\varepsilon \sim \mathcal{N}(0, 10^{-4})$ is used to equip the set with non-zero measure, as used in [Phillips et al., 2022]. We choose the function-valued Brownian process as the unconditional process since its derived bridge has a closed form. We choose the bounded grid of $[-1, 1]$ to evaluate the function, and the grid is uniformly discretized into a finite number of points, as shown in Figure 3a. Since the SDE is defined in H , such discretization stands for choosing a finite base and projecting it into the finite dimension. However, the projected process should be consistent under arbitrary discretizations. We show it by training the neural operator under a low-resolution scheme (8 points distributed within $[-1, 1]$) and evaluate it in a high-resolution case (128 points). Note that our learned bridge (Figure 3b) shows high consistency with the ground true Brownian bridge (Figure 3c), even in a much finer grid. We also compared the MSE between the simulated trajectories by the true score and the estimated one with the same random seed initialization. The results indicate that the learned process is discretization-invariant, i.e., it represents the infinite-dimensional process. We further study the model’s performance under different discretization levels, as shown in Figure 3d; we observe that the model shows great consistency under discretizations in terms of the MSE metrics. More samples from the estimated bridge can be found in Figure 7

Circles: We further test our method by simulating the Brownian bridge between 2D circles, which acts as the simplest 2D stochastic shape bridge and holds a known form that we can compare. We shall see in the next experiment the true shape bridge is inaccessible. The Circle can be treated as a function from \mathbb{R} to \mathbb{R}^2 , and can be characterized by finite points along the outlines. We are trying to bridge two circles with different radii. Figure 4a gives a visualization of the forward unconditional process. Then we train the model with only 16 points evenly sampled from the circle and evaluate it in higher resolutions (See Figure 4b and 8). Also, Figure 4c shows the ground true bridge simulated

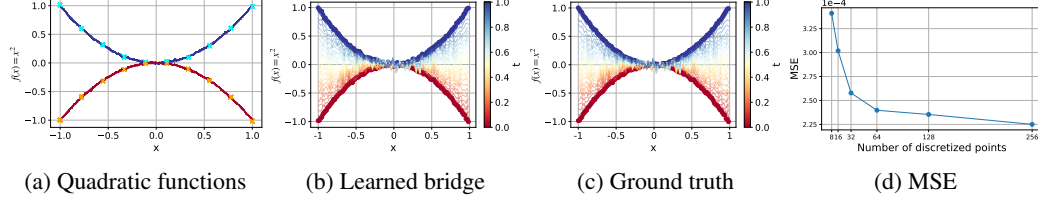


Figure 3: Qualitative results for Brownian bridges between two quadratic functions; (a) Two quadratic functions are chosen as the starting ($f(x) = x^2 + \varepsilon$, blue) and the target ($f(x) = -x^2 + \varepsilon$, red). Both are evaluated at 8 points evenly distributed within $[-1, 1]$ for training (marked in cyan and orange respectively); (b) One sample from the learned reversed Brownian bridge, evaluated at 128 evenly distributed points; (c) One sample from the true reversed Brownian bridge, simulated with the same random seed as (b) for comparison; (d) MSE between the estimated and the true bridges under different resolutions.

with the same random seed, and we could expect consistency between these two simulations. Besides the visual inspection, we show the score output at different stages of the process since we have access to the ground true score that we can compare. The results are shown in Figure 5. Since, in the Brownian case, there is no drift term in the unconditional process, the additional drift introduced by the transformation is the only force that drives the functions toward the target, which is reflected in the visualization that the score arrows should always point toward the center, despite of the discretization, which can be observed in the Figure 5 as well.

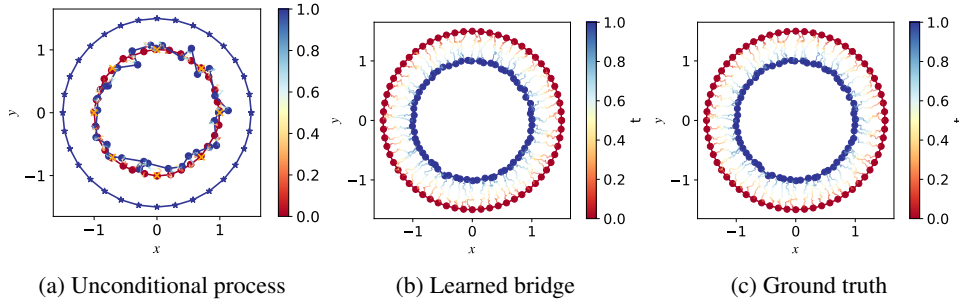


Figure 4: Qualitative results for Brownian bridges between two circles; (a) The unconditional forward process starting from the red circle discretized into 32 points, the training uses 16 points marked in orange crosses; (b) One sample from the learned reversed Brownian bridge, evaluated at 128 evenly distributed points; (c) One sample from the true reversed Brownian bridge, simulated with the same random seed as (b) for comparison.

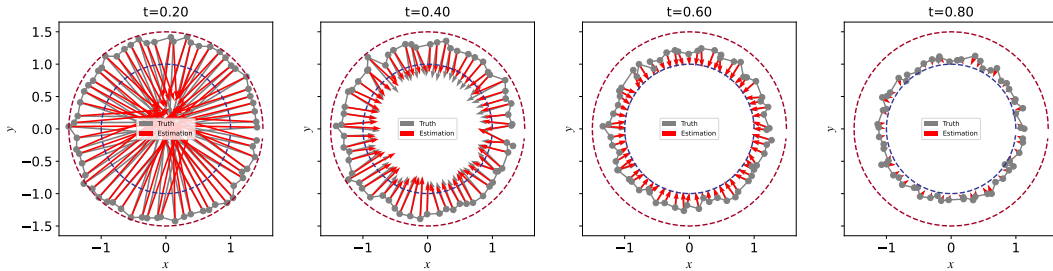


Figure 5: The inspections of the estimated score and the true score at different time steps of the bridge process.

5.2 Biological shape evolution

We finally evaluate our method on real data. Specifically, we are interested in modeling the stochastic change in butterfly morphometry over time. In the phylogenetic analysis, such bridge processes model the transitions along the edge between nodes in a phylogenetic tree, where the nodes store the

observed data that comes from specimens. Developing the fast bridge simulation approach facilitates large-scale phylogenetic tree simulation and biological inferences. However, when modeling the shape, the linear process can not be directly applied since the topology of the shape must be preserved. We detail our nonlinear setting for the shape process in B.4. By applying the proposed method, we can now bridge between two butterfly shapes. It’s worth noticing that the bridge is constructed in infinite rather than finite dimensions. To prove this, we only train the score approximator with 32 points, corresponding to a finite discretization of the shape function. During the inference, we evaluate the bridge on different levels of discretization, and it shows that the approximator can give reasonably enough interpolations between low-discretized points, as shown in Figure 6. We point out that our method does not constrain a specific shape since the deformation of the shape is modeled instead of the shape itself. Also, since the bridge is constructed between two sets with non-zero measures, in practice, it allows the observation to contain noise. Both these features make our method suitable for modeling stochastic biological shape evolution, where 1) Multiple similar shapes are considered, and 2) The observations often contain noise. We test our model on more butterfly species which are close on the phylogenetic tree, the results are shown in Figure 9 and 10. This marks the first instance where the simulation of nonlinear diffusion shape bridges has been achieved using a discretization-invariant method, to the best of our knowledge.

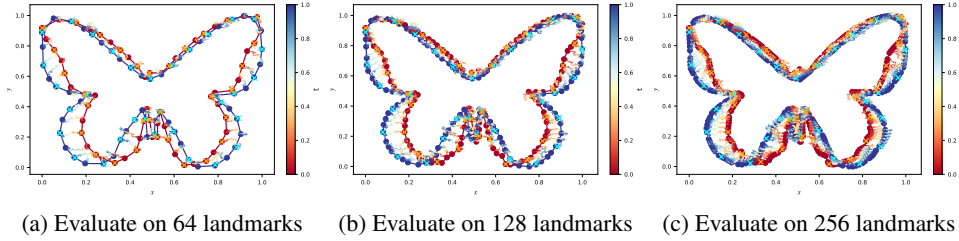


Figure 6: The stochastic shape bridge between two butterfly shapes (Papilio polytes in red, Parnassius honrathi in blue). The shape is represented by landmarks of different numbers. Our method only needs to train on a few sample points (marked in cyan and orange crosses) and can generalize to arbitrary resolutions.

6 Conclusion

We introduce a novel approach for simulating nonlinear diffusion bridges in infinite-dimensional spaces. This method utilizes Doob’s h -transform applied to an unconditional process, transforming it into a conditional diffusion bridge. Subsequently, we reverse this bridge in time and simulate the reversed sequence using a drift learned from the original, unconditional process. Utilizing a neural operator, we establish that this learned drift retains continuity across discretizations, affirming its role as a discretization-invariant representation of the underlying infinite-dimensional dynamics. We validate our approach through several functional diffusion bridge test cases, especially the phylogenetic shape analysis problem, where our method showcases its effectiveness of high-resolution zero-shot training and generalization to various shapes, together with robustness under different levels of discretizations.

However, simulating the time-reversed bridge poses computational challenges, particularly the necessity of calculating the Jacobian of a . As outlined in Heng et al. [2021], learning the forward bridge typically involves repeated sampling from the reverse bridge, which significantly escalates computational costs. To address these issues, we aim to develop a method that directly learns the forward bridge, thereby bypassing the need for reversal. We also anticipate applying this approach to additional applications, such as stochastic image alignment and other contexts involving continuous data, to further validate its versatility and effectiveness.

References

- Jian Qing Shi and Taeryon Choi. *Gaussian process regression analysis for functional data*. CRC press, 2011.
- Leonard CG Rogers and David Williams. *Diffusions, markov processes, and martingales: Volume 1, foundations*, volume 1. Cambridge university press, 2000.
- Giulio Franzese, Giulio Corallo, Simone Rossi, Markus Heinonen, Maurizio Filippone, and Pietro Michiardi. Continuous-time functional diffusion processes. *Advances in Neural Information Processing Systems*, 36, 2024.
- Jae Hyun Lim, Nikola B Kovachki, Ricardo Baptista, Christopher Beckham, Kamyar Azizzadenesheli, Jean Kossaifi, Vikram Voleti, Jiaming Song, Karsten Kreis, Jan Kautz, et al. Score-based diffusion models in function space. *arXiv preprint arXiv:2302.07400*, 2023.
- Jakiw Pidstrigach, Youssef Marzouk, Sebastian Reich, and Sven Wang. Infinite-dimensional diffusion models for function spaces. *arXiv e-prints*, pages arXiv–2302, 2023.
- Aapo Hyvärinen and Peter Dayan. Estimation of non-normalized statistical models by score matching. *Journal of Machine Learning Research*, 6(4), 2005.
- Pascal Vincent. A connection between score matching and denoising autoencoders. *Neural computation*, 23(7):1661–1674, 2011.
- Yang Song, Jascha Sohl-Dickstein, Diederik P Kingma, Abhishek Kumar, Stefano Ermon, and Ben Poole. Score-based generative modeling through stochastic differential equations. *International Conference on Learning Representations*, 2020.
- Chin-Wei Huang, Jae Hyun Lim, and Aaron C Courville. A variational perspective on diffusion-based generative models and score matching. *Advances in Neural Information Processing Systems*, 34: 22863–22876, 2021.
- Elizabeth Louise Baker, Gefan Yang, Michael L Severinsen, Christy Anna Hipsley, and Stefan Sommer. Conditioning non-linear and infinite-dimensional diffusion processes. *arXiv preprint arXiv:2402.01434*, 2024.
- Bernard Delyon and Ying Hu. Simulation of conditioned diffusion and application to parameter estimation. *Stochastic Processes and their Applications*, 116(11):1660–1675, 2006.
- Moritz Schauer, Frank van der Meulen, and Harry van Zanten. Guided proposals for simulating multi-dimensional diffusion bridges. *Bernoulli*, 23(4A), November 2017. ISSN 1350-7265. doi: 10.3150/16-bej833. URL <http://dx.doi.org/10.3150/16-BEJ833>.
- Jeremy Heng, Valentin De Bortoli, Arnaud Doucet, and James Thornton. Simulating diffusion bridges with score matching. *arXiv preprint arXiv:2111.07243*, 2021.
- Yesom Park, Jaemoo Choi, Changyeon Yoon, Myungjoo Kang, et al. Learning pde solution operator for continuous modeling of time-series. *arXiv preprint arXiv:2302.00854*, 2023.
- Md Ashiqur Rahman, Zachary E Ross, and Kamyar Azizzadenesheli. U-no: U-shaped neural operators. *arXiv e-prints*, pages arXiv–2204, 2022.
- Frank Van der Meulen and Moritz Schauer. Automatic backward filtering forward guiding for markov processes and graphical models. *arXiv preprint arXiv:2010.03509*, 2020.
- Marc Corstanje, Frank van der Meulen, Moritz Schauer, and Stefan Sommer. Simulating conditioned diffusions on manifolds. *arXiv preprint arXiv:2403.05409*, 2024.
- Jascha Sohl-Dickstein, Eric Weiss, Niru Maheswaranathan, and Surya Ganguli. Deep unsupervised learning using nonequilibrium thermodynamics. In *International conference on machine learning*, pages 2256–2265. PMLR, 2015.
- Yang Song and Stefano Ermon. Generative modeling by estimating gradients of the data distribution. *Advances in neural information processing systems*, 32, 2019.

- Yang Song, Jascha Sohl-Dickstein, Diederik P Kingma, Abhishek Kumar, Stefano Ermon, and Ben Poole. Score-based generative modeling through stochastic differential equations. In *International Conference on Learning Representations*, 2021. URL <https://openreview.net/forum?id=PxTIG12RRHS>.
- Lorenzo Baldassari, Ali Siahkoobi, Josselin Garnier, Knut Solna, and Maarten V de Hoop. Conditional score-based diffusion models for bayesian inference in infinite dimensions. *Advances in Neural Information Processing Systems*, 36, 2024.
- Paul Hagemann, Sophie Mildener, Lars Ruthotto, Gabriele Steidl, and Nicole Tianjiao Yang. Multilevel diffusion: Infinite dimensional score-based diffusion models for image generation. *arXiv preprint arXiv:2303.04772*, 2023.
- Valentin De Bortoli, James Thornton, Jeremy Heng, and Arnaud Doucet. Diffusion schrödinger bridge with applications to score-based generative modeling. *Advances in Neural Information Processing Systems*, 34:17695–17709, 2021.
- Yuyang Shi, Valentin De Bortoli, Andrew Campbell, and Arnaud Doucet. Diffusion schrödinger bridge matching. *Advances in Neural Information Processing Systems*, 36, 2024.
- Zhicong Tang, Tiankai Hang, Shuyang Gu, Dong Chen, and Baining Guo. Simplified diffusion schrödinger bridge. *arXiv preprint arXiv:2403.14623*, 2024.
- James Thornton, Michael Hutchinson, Emile Mathieu, Valentin De Bortoli, Yee Whye Teh, and Arnaud Doucet. Riemannian diffusion schrödinger bridge. *arXiv preprint arXiv:2207.03024*, 2022.
- Ulrich G Haussmann and Etienne Pardoux. Time reversal of diffusions. *The Annals of Probability*, pages 1188–1205, 1986.
- Annie Millet, David Nualart, and Marta Sanz. Time reversal for infinite-dimensional diffusions. *Probability theory and related fields*, 82(3):315–347, 1989.
- Guan-Hong Liu, Arash Vahdat, De-An Huang, Evangelos A Theodorou, Weili Nie, and Anima Anandkumar. I2sb: Image-to-image schrödinger bridge. *arXiv preprint arXiv:2302.05872*, 2023a.
- Mauricio Delbracio and Peyman Milanfar. Inversion by direct iteration: An alternative to denoising diffusion for image restoration. *arXiv preprint arXiv:2303.11435*, 2023.
- Zongyi Li, Nikola Borislavov Kovachki, Kamyar Azizzadenesheli, Kaushik Bhattacharya, Andrew Stuart, Anima Anandkumar, et al. Fourier neural operator for parametric partial differential equations. In *International Conference on Learning Representations*, 2020a.
- Zongyi Li, Nikola Kovachki, Kamyar Azizzadenesheli, Burigede Liu, Kaushik Bhattacharya, Andrew Stuart, and Anima Anandkumar. Neural operator: Graph kernel network for partial differential equations. *arXiv preprint arXiv:2003.03485*, 2020b.
- Lu Lu, Pengzhan Jin, Guofei Pang, Zhongqiang Zhang, and George Em Karniadakis. Learning nonlinear operators via deepnet based on the universal approximation theorem of operators. *Nature machine intelligence*, 3(3):218–229, 2021.
- Nikola Kovachki, Zongyi Li, Burigede Liu, Kamyar Azizzadenesheli, Kaushik Bhattacharya, Andrew Stuart, and Anima Anandkumar. Neural operator: Learning maps between function spaces with applications to pdes. *Journal of Machine Learning Research*, 24(89):1–97, 2023.
- Ashish Vaswani, Noam Shazeer, Niki Parmar, Jakob Uszkoreit, Llion Jones, Aidan N Gomez, Łukasz Kaiser, and Illia Polosukhin. Attention is all you need. *Advances in neural information processing systems*, 30, 2017.
- Mustafa Bayram, Tugcem Partal, and Gulsen Orucova Buyukoz. Numerical methods for simulation of stochastic differential equations. *Advances in Difference Equations*, 2018:1–10, 2018.
- Angus Phillips, Thomas Seror, Michael Hutchinson, Valentin De Bortoli, Arnaud Doucet, and Emile Mathieu. Spectral diffusion processes. *arXiv preprint arXiv:2209.14125*, 2022.

- Giuseppe Da Prato and Jerzy Zabczyk. *Stochastic equations in infinite dimensions*. Cambridge university press, 2014.
- Wilfried Loges. Girsanov’s theorem in hilbert space and an application to the statistics of hilbert space-valued stochastic differential equations. *Stochastic processes and their applications*, 17(2): 243–263, 1984.
- Laurent Younes. *Shapes and diffeomorphisms*, volume 171. Springer, 2010.
- Martin Bauer, Martins Bruveris, and Peter W Michor. Overview of the geometries of shape spaces and diffeomorphism groups. *Journal of Mathematical Imaging and Vision*, 50:60–97, 2014.
- Hiroshi Kunita and Hiroshi Kunita. *Stochastic flows and stochastic differential equations*, volume 24. Cambridge university press, 1990.
- GBIF.Org User. Occurrence download, 2024. URL <https://www.gbif.org/occurrence/download/0075323-231120084113126>.
- Alexander Kirillov, Eric Mintun, Nikhila Ravi, Hanzi Mao, Chloe Rolland, Laura Gustafson, Tete Xiao, Spencer Whitehead, Alexander C Berg, Wan-Yen Lo, et al. Segment anything. In *Proceedings of the IEEE/CVF International Conference on Computer Vision*, pages 4015–4026, 2023.
- Shilong Liu, Zhaoyang Zeng, Tianhe Ren, Feng Li, Hao Zhang, Jie Yang, Chunyuan Li, Jianwei Yang, Hang Su, Jun Zhu, et al. Grounding dino: Marrying dino with grounded pre-training for open-set object detection. *arXiv preprint arXiv:2303.05499*, 2023b.
- Dean C Adams and Erik Otárola-Castillo. geomorph: an r package for the collection and analysis of geometric morphometric shape data. *Methods in ecology and evolution*, 4(4):393–399, 2013.

A Proofs

In this section, we provide the proofs for two theorems in the paper.

A.1 Proof of Theorem 3.1

Proof. We follow the setup in Millet et al. [1989]. Let $I(i) \subset \mathbb{Z}, \forall i \in \mathbb{Z}$ be a finite set of indices, $\{e_i\}_{i=1}^\infty$ be an orthonormal basis for $H \ni X(t)$, and $\{k_j\}_{j=1}^\infty$ be an orthonormal basis for $U \ni W(t)$. Then we split $X(t)$ into an infinite number of finite vectors; specifically, we denote $X^i(t) = (X_j(t), j \in I(i)) \in \mathbb{R}^I$ to be the vector consisting of all the components of X indexed by the entries in $I(i)$, with $X_j(t) = \langle X(t), e_j \rangle_H$. Similarly, let $\hat{X}^i(t) = (X_j(t), j \notin I(i))$ be the complement of $X^i(t)$. Then, by assumption, the conditional law of $X^i(t)$ given its complement $\hat{X}^i(t) = \xi^i$ has a density $p_t(x_i | \xi^i)$.

Consider the conditional bridge process (2), written in terms of the bases $\{e_i\}$ and $\{k_j\}$:

$$dX_i^c(t) = [f(t, X^c(t)) + a(t, X^c(t)) \nabla \log h(t, X^c(t))]_i dt + \sum_{j=1}^\infty g_{ij}(t, X^c(t)) dW_j(t). \quad (16)$$

We apply the time reversal theorem [Millet et al., 1989], to obtain the reversed bridge $Y^c(t)$:

$$dY_i^c(t) = -[f(T-t, Y^c(t))]_i dt - [a(T-t, Y^c(t)) \nabla \log h(T-t, Y^c(t))]_i dt \quad (17a)$$

$$+ \left[\frac{1}{p_t(Y^{c,i}(t) | \hat{Y}^{c,i}(t))} \sum_{j \in I(i)} \nabla_j [a_{ij}(T-t, Y^c(t)) p_t(Y^{c,i}(t) | \hat{Y}^{c,i}(t))] \right]_i dt \quad (17b)$$

$$+ \sum_{j=1}^\infty g_{ij}(T-t, Y^c(t)) dB_j(t). \quad (17c)$$

In order to write this in the form appearing in the theorem, we focus on the second term. By properties of the Fréchet derivative, it holds that

$$\frac{1}{p_t(Y^{c,i}(t) | \hat{Y}^{c,i}(t))} \sum_{j \in I(i)} \nabla_j [a_{ij}(T-t, Y(t)) p_t(Y^{c,i}(t) | \hat{Y}^{c,i}(t))] \quad (18a)$$

$$= \sum_{j \in I(i)} \nabla_j [a_{ij}(T-t, Y(t))] \quad (18b)$$

$$+ \frac{1}{p_t(Y^{c,i}(t) | \hat{Y}^{c,i}(t))} \sum_{j \in I(i)} a_{ij}(T-t, Y(t)) \nabla_j [p_t(Y^{c,i}(t) | \hat{Y}^{c,i}(t))] \quad (18c)$$

$$= \sum_{j \in I(i)} \nabla_j [a_{ij}(T-t, Y(t))] + \sum_{j \in I(i)} a_{ij}(T-t, Y(t)) \nabla_j \log [p_t(Y^{c,i}(t) | \hat{Y}^{c,i}(t))]. \quad (18d)$$

We now compare this to the second term by expanding that. Given $h(T-t, Y(t)) = \mathbb{P}(Y(T) | Y(t))$, we expand it using conditional densities:

$$\mathbb{P}(Y^c(T) | Y^c(t)) = \sum_i^\infty p_{T|t}(Y^{c,i}(T) | Y^{c,i}(t), \hat{Y}^{c,i}(t), \hat{Y}^{c,i}(T)) \quad (19)$$

Therefore,

$$\begin{aligned} & [a(T-t, Y^c(t)) \nabla \log h(T-t, Y^c(t))]_i \\ &= \sum_{j \in I(i)} a_{ij}(T-t, Y^c(t)) \nabla_j \log p_{T|t}(Y^{c,i}(T) | Y^{c,i}(t), \hat{Y}^{c,i}(t), \hat{Y}^{c,i}(T)) \end{aligned} \quad (20)$$

Note that $p_t(Y^{c,i}(t) \mid \hat{Y}^{c,i}(t))$ is a marginal density over $0, T$, thereby can be written as:

$$p_t(Y^{c,i}(t) \mid \hat{Y}^{c,i}(t)) \quad (21a)$$

$$= p_t(Y^{c,i}(t) \mid \hat{Y}^{c,i}(t), Y^{c,i}(0), \hat{Y}^{c,i}(0), Y^{c,i}(T), \hat{Y}^{c,i}(T)) \quad (21b)$$

$$= \frac{p_{t|0}(Y^{c,i}(t) \mid \hat{Y}^{c,i}(t), Y^{c,i}(0) \mid \hat{Y}^{c,i}(0)) p_{T|t}(Y^{c,i}(T) \mid \hat{Y}^{c,i}(T), Y^{c,i}(t) \mid \hat{Y}^{c,i}(t))}{p_{T|0}(Y^{c,i}(T) \mid \hat{Y}^{c,i}(T), Y^{c,i}(0) \mid \hat{Y}^{c,i}(0))} \quad (21c)$$

Taking the logarithm and the gradient with respect to $Y^{c,i}(t)$, we obtain:

$$\nabla_{Y^{c,i}(t)} \log p_t(Y^{c,i}(t) \mid \hat{Y}^{c,i}(t)) \quad (22a)$$

$$= \nabla_{Y^{c,i}(t)} \log p_{t|0}(Y^{c,i}(t) \mid \hat{Y}^{c,i}(t), Y^{c,i}(0), \hat{Y}^{c,i}(0)) \quad (22b)$$

$$+ \nabla_{Y^{c,i}(t)} \log p_{T|t}(Y^{c,i}(T) \mid \hat{Y}^{c,i}(T), Y^{c,i}(t), \hat{Y}^{c,i}(t)) \quad (22c)$$

Therefore, the reversed bridge can be written with respect to the bases:

$$dY_i^c(t) \quad (23a)$$

$$= \left[-f(T-t, Y^c(t)) + \sum_{j \in I(i)} \nabla_{Y^{c,i}(t)} a_{ij}(T-t, Y^c(t)) \right. \quad (23b)$$

$$\left. - \sum_{j \in I(i)} a_{ij}(T-t, Y^c(t)) \nabla_{Y^{c,i}(t)} \log p_{t|0}(Y^{c,i}(t) \mid \hat{Y}^{c,i}(t), Y^{c,i}(0), \hat{Y}^{c,i}(t)) \right] dt \quad (23c)$$

$$+ \sum_{j=1}^{\infty} g_{ij}(T-t, Y^c(t)) dB_j(t) \quad (23d)$$

By summing over indices i , we obtain the infinite-dimensional reversed bridge as shown in Theorem 3.1. \square

A.2 Proof of Theorem 4.1

Proof. We first compute the Radon-Nikodym derivative of \mathbb{P}^{x_0} with respect to $\mathbb{Q}_\theta^{x_0}$ by Girsanov's theorem (See Da Prato and Zabczyk [2014], Theorem 10.14, Lemma 10.15, also see Loges [1984] Theorem 2), which states that there exists a U -valued stochastic process $\psi(t, Y(t))$ that satisfies

$$g(t, Y(t)) C^{1/2} \psi(t, Y(t)) = \tilde{f}(t, Y(t)) - f_\theta(t, Y(t)), \quad (24)$$

such that,

$$\frac{d\mathbb{P}^{x_0}}{d\mathbb{Q}_\theta^{x_0}}(Y(t)) = \exp \left\{ \int_0^T \|\psi(t, Y(t))\|_U dB(t) - \frac{1}{2} \int_0^T \|\psi(t, Y(t))\|_U^2 dt \right\}$$

Thus, the KL divergence is:

$$D_{KL}(\mathbb{P}^{x_0} \mid \mathbb{Q}_\theta^{x_0}) \quad (25a)$$

$$= \mathbb{E}_{Y(t)} \left\{ \int_0^T \|\psi(t, Y(t))\|_U dB(t) \right\} + \mathbb{E}_{Y(t)} \left\{ -\frac{1}{2} \int_0^T \|\psi(t, Y(t))\|_U^2 dt \right\} \quad (25b)$$

$$= \mathbb{E}_{X(t)} \left\{ \frac{1}{2} \int_0^T \|\psi(t, X(t))\|_U^2 dt \right\} \quad (25c)$$

$$= \mathbb{E}_{X(t)} \left\{ \frac{1}{2} \int_0^T \left\| C^{-1/2} g^{-1}(t, X(t)) \left\{ \tilde{f}(t, X(t)) - f_\theta(t, X(t)) \right\} \right\|_U^2 dt \right\} \quad (25d)$$

$$= \mathbb{E}_{X(t)} \left\{ \frac{1}{2} \int_0^T \left\| C^{-1/2} g^{-1}(t, X(t)) \left\{ a(t, X(t)) \nabla \log \tilde{h}(t, X(t)) - \mathcal{G}_\theta(t, X(t)) \right\} \right\|_U^2 dt \right\} \quad (25e)$$

In the second equation, the first term vanishes because of the martingale property of the Itô integral, while the second term flips the sign because of the change of process from $Y(t)$ to $X(t)$ with the reversed time variable. Denote $C^{-1/2}g^{-1}(t, x)$ by $A_t(x)$ for short, expand the squared norm in (25):

$$D_{KL}(\mathbb{P}^{x_0} \mid \mathbb{Q}_\theta^{x_0}) = \mathbb{E}_{X(t)} \left\{ \frac{1}{2} \int_0^T \left\| A_t(X(t)) \left\{ a(t, X(t)) \nabla \log \tilde{h}(t, X(t)) - \mathcal{G}_\theta(t, X(t)) \right\} \right\|_U^2 dt \right\} \quad (26a)$$

$$= \frac{1}{2} \int_0^T \int_H \left\| A_t(x) \left\{ a(t, x) \nabla \log \tilde{h}(t, x) - \mathcal{G}_\theta(t, x) \right\} \right\|_U^2 d\mu_t(dx) dt \quad (26b)$$

$$= \frac{1}{2} \int_0^T \underbrace{\int_H \|A_t(x) \mathcal{G}_\theta(t, x)\|_U^2 d\mu_t(dx)}_{C_1} dt \quad (26c)$$

$$+ \frac{1}{2} \int_0^T \underbrace{\int_H \|A_t(x) a(t, x) \nabla \log \tilde{h}(t, x)\|_U^2 d\mu_t(dx)}_{C_2} dt \quad (26d)$$

$$- \underbrace{\int_0^T \int_H \langle A_t(x) \mathcal{G}_\theta(t, x), A_t(x) a(t, x) \nabla \log \tilde{h}(t, x) \rangle_U d\mu_t(dx) dt}_{C_3} \quad (26e)$$

where $d\mu_t(dx)$ denotes $\mathbb{P}^{x_0}(X(t) \in dx \mid X(0)) = P(0, x_0, t, dx)$. Under the given partition $(t_i)_{i=1}^I$ of $[0, T]$, we shall split the time integral in C_3 by finite parts:

$$C_3 = \sum_{i=1}^I \int_{t_{i-1}}^{t_i} \int_H \langle A_t(x) \mathcal{G}_\theta(t, x), A_t(x) a(t, x) \nabla \log \tilde{h}(t, x) \rangle_U d\mu_t(dx) dt \quad (27a)$$

$$= \sum_{i=1}^I \int_{t_{i-1}}^{t_i} \int_H \langle A_t(x) \mathcal{G}_\theta(t, x), A_t(x) a(t, x) \nabla \log P(0, x_0, t, dx) \rangle_U P(0, x_0, t, dx) dt \quad (27b)$$

$$= \sum_{i=1}^I \int_{t_{i-1}}^{t_i} \int_H \langle A_t(x) \mathcal{G}_\theta(t, x), A_t(x) a(t, x) \nabla P(0, x_0, t, dx) \rangle_U dt \quad (27c)$$

Using the Chapman-Kolmogorov equation [Da Prato and Zabczyk, 2014, Corollary 9.15], for any $0 \leq t_{i-1} < t \leq T$, we show:

$$\nabla P(0, x_0, t, dx) = \nabla_{X(t)} \int_H P(0, x_0, t_{i-1}, dx_{t_{i-1}}) P(t_{i-1}, x_{t_{i-1}}, t, dx) \quad (28a)$$

$$= \int_H \nabla_{X(t)} P(t_{i-1}, x_{t_{i-1}}, t, dx) P(0, x_0, t_{i-1}, dx_{t_{i-1}}) \quad (28b)$$

$$= \int_H \nabla_{X(t)} \log P(t_{i-1}, x_{t_{i-1}}, t, dx) P(t_{i-1}, x_{t_{i-1}}, t, dx) P(0, x_0, t_{i-1}, dx_{t_{i-1}}) \quad (28c)$$

Therefore, substitute (28) back into (27)

$$C_3 = \sum_{i=1}^I \int_{t_{i-1}}^{t_i} dt \int_H P(t_{i-1}, x_{t_{i-1}}, t, dx) P(0, x_0, t_{i-1}, dx_{t_{i-1}}) \quad (29a)$$

$$\int_H \langle A_t(x) \mathcal{G}_\theta(t, x), A_t(x) a(t, x) \nabla \log P(t_{i-1}, x_{t_{i-1}}, t, dx) \rangle_U \quad (29b)$$

$$= \sum_{i=1}^I \int_{t_{i-1}}^{t_i} dt P(0, x_0, t, dx) \int_H \langle A_t(x) \mathcal{G}_\theta(t, x), A_t(x) a(t, x) \nabla \log P(t_{i-1}, x_{t_{i-1}}, t, dx) \rangle_U \quad (29c)$$

$$= \sum_{i=1}^I \int_{t_{i-1}}^{t_i} \int_H \langle A_t(x) \mathcal{G}_\theta(t, x_t), A_t(x) a(t, x) \nabla \log P(t_{i-1}, x_{t_{i-1}}, t, dx) \rangle_U d\mu_t(dx) dt \quad (29d)$$

We then claim that:

$$L(\theta) := \frac{1}{2} \sum_{i=1}^I \int_{t_{i-1}}^{t_i} \mathbb{E}_{X(t)} \{ \|A_t(x) \{ \mathcal{G}_\theta(t, x) - b(t, x, t_{i-1}, x_{t_{i-1}}) \} \|_U^2 \} dt = C_1 + C_4 - C_3$$

where

$$C_4 = \frac{1}{2} \sum_{i=1}^I \int_{t_{i-1}}^{t_i} \int_H \|A_t(x) a(t, x) \nabla \log P(t_{i-1}, x_{t_{i-1}}, t, dx)\|_U^2 d\mu_t(dx) dt$$

To show that, we expand the squared norm and get:

$$L(\theta) = \underbrace{\frac{1}{2} \sum_{i=1}^I \int_{t_{i-1}}^{t_i} \int_H \|A_t(x) \mathcal{G}_\theta(t, x)\|_U^2 d\mu_t(dx) dt}_{C_1} \quad (30a)$$

$$+ \underbrace{\frac{1}{2} \sum_{i=1}^I \int_{t_{i-1}}^{t_i} \int_H \|A_t(x) a(t, x_t) \nabla \log P(t_{i-1}, x_{t_{i-1}}, t, dx)\|_U^2 d\mu_t(dx) dt}_{C_4} \quad (30b)$$

$$- \underbrace{\sum_{i=1}^I \int_{t_{i-1}}^{t_i} \int_H \langle A_t(x) \mathcal{G}_\theta(t, x), A_t(x) a(t, x) \nabla \log P(t_{i-1}, x_{t_{i-1}}, t, dx) \rangle_H d\mu_t(dx) dt}_{C_3} \quad (30c)$$

Finally, by comparing with (26) and taking $C = C_4 - C_2$, we finish the proof. \square

B Experiment Details

In this section, we provide the general algorithms for training and evaluating the model, also more details on the three experiments. All the experiments are done on the platform with one NVIDIA RTX 4090 GPU and Intel(R) Xeon(R) CPU E5-2650 v4 @ 2.20GHz with 128GB memory and Ubuntu 22.04.4 LTS OS. The codes are available on <https://github.com/bookdiver/scoreoperator>

B.1 Algorithms

B.2 Quadratic functions

We model the stochastic dynamics in the function space as the Brownian motion:

$$dX(t) = \sigma dW(t) \quad (31)$$

with $\sigma = 0.1$, which has a closed-form time-reversed bridge:

$$dY(t) = \sigma^2 \frac{y_T - Y(t)}{T - t} dt + \sigma dB(t) \quad (32)$$

We designed our operator to have 6 Fourier layers. The details are shown in Table 1. We train with 10,000 i.i.d. batched samples and with a batch size of 16. We chose the Adam optimizer with an initial learning rate of 0.001 and cosine decay to $1e-5$ as 80% of the training is finished.

Algorithm 1 Training

Require: Bridging object measure μ_0^d **Require:** Total time length T , time step δt **Require:** Batch size B **Require:** Initialized \mathcal{G}_θ **Require:** Drift term f^d , diffusion term g^d

```

1: Form discrete time grid  $\{t_0 = 0, t_1, \dots, t_{n-1}, t_n = T\}, n = \lfloor T/\delta t \rfloor$ 
2: while Not converged do
3:   Sample  $\{X_j^d(0)\}_{j=1}^B \sim \mu_0^d$ , i.i.d.
4:   for  $do i \leftarrow 1, \dots, n$ 
5:     Sample  $\{\varepsilon_j\}_{j=1}^B \sim \mathcal{N}(0, I_k)$ , i.i.d
6:     for  $do j \leftarrow 1, \dots, B$ 
7:        $X_j^d(t_i) \leftarrow X_j^d(t_{i-1}) + f^d(t_{i-1}, X_j^d(t_{i-1}))\delta t + g^d(t_{i-1}, X_j^d(t_{i-1}))\varepsilon_j$ 
8:        $b_j^d(t_i, X_j^d(t_i), t_{i-1}, X_j^d(t_{i-1})) \leftarrow -g^d(t_{i-1}, X_j^d(t_{i-1}))\varepsilon_j/\delta t$ 
9:     end for
10:   end for
11:    $L^d(\theta) = \frac{1}{2B}\delta t \sum_{j=1}^B \sum_{i=1}^n \|\mathcal{G}_\theta(t_i, X_j^d(t_i)) - b_j^d(t_i, X_j^d(t_i), t_{i-1}, X_j^d(t_{i-1}))\|^2$ 
12:   Perform gradient descent step on  $L^d(\theta)$ 
13: end while

```

Algorithm 2 Inference

Require: Bridging object measures μ_T^d **Require:** Total time length T , time step δt **Require:** Pretrained \mathcal{G}_θ **Require:** Drift term f^d , diffusion term g^d

```

1: Form discrete time grid  $\{t_0 = 0, t_1, \dots, t_{n-1}, t_n = T\}, n = \lfloor T/\delta t \rfloor$ 
2: Sample  $X^{(c)d}(T) \sim \mu_T^d$ , i.i.d.
3: for  $do i \leftarrow n, \dots, 1$ 
4:   Sample  $\varepsilon \sim \mathcal{N}(0, I_k)$ , i.i.d
5:    $X^{(c)d}(t_{i-1}) \leftarrow X^{(c)d}(t_i) + \{f^d(t_i, X^{(c)d}(t_i)) + \mathcal{G}_\theta(t_i, X^{(c)d}(t_i)) + \nabla \cdot (g^d(g^d)^T)(t_i, X^{(c)d}(t_i))\}\delta t + g^d(t_i, X^{(c)d}(t_i))\varepsilon$ 
6: end for

```

B.3 Circles

The SDE of circles follows the same as the one in the quadratic function experiment. The bigger circle has a radius of 1.5, and the smaller circle has a radius of 1.0. For the neural operator design, it is shown in Table 2. We train with 10,000 i.i.d. batched samples and with a batch size of 16. We chose the Adam optimizer with an initial learning rate of 0.001 and cosine decay to 1e-5 as 80% of the training is finished.

B.4 Butterflies

We shall first briefly review the stochastic shape analysis. A shape $s : \mathbb{R}^d \rightarrow \mathbb{R}^d$ is usually modeled as an embedding in \mathbb{R}^d [Younes, 2010]. Matching two shapes s_0, s_T along time is achieved by finding a diffeomorphism $f : [0, T] \times \mathbb{R}^d \rightarrow \mathbb{R}^d$, such that $f(0, s_0(\xi)) = s_0(\xi)$ and $f(T, s_0(\xi)) = s_T(\xi)$ for any $\xi \in \mathbb{R}^n$. There are normally infinitely many numbers of such f s that suffice, while only the one with the lowest energy is considered, corresponding to the “simplest” deterministic transformation between the shapes. Finding such a diffeomorphism is achieved by optimizing a given energy functional [Bauer et al., 2014]. However, we are more interested in the stochastic transformation between the shapes, that is, f follows a function-valued SDE that conditions on hitting close enough to $f(T) : s_0(\xi) \mapsto s_T(\xi)$ with the starting point as $f_0 = \text{id}$. One way of defining f is by the displacement of the shape, that is, $f(t, s_0(\xi)) = X(t, \xi) + s_0(\xi), x \in \mathbb{R}^d$, where $X \in L^2([0, T] \times \mathbb{R}^d, \mathbb{R}^d)$ is a random variable in Hilbert space. It is easy to show that

Layer	Input	Output	Grid size	Fourier modes	Activation
Lifting	$u : \mathbb{R} \rightarrow \mathbb{R}$	$v_0 : \mathbb{R} \rightarrow \mathbb{R}^{16}$	8	-	-
Down1	$v_0 : \mathbb{R} \rightarrow \mathbb{R}^{16}$	$v_1 : \mathbb{R} \rightarrow \mathbb{R}^{16}$	8	6	GeLU
Down2	$v_1 : \mathbb{R} \rightarrow \mathbb{R}^{16}$	$v_2 : \mathbb{R} \rightarrow \mathbb{R}^{32}$	4	4	GeLU
Down3	$v_2 : \mathbb{R} \rightarrow \mathbb{R}^{32}$	$v_3 : \mathbb{R} \rightarrow \mathbb{R}^{64}$	2	2	GeLU
Up1	$v_3 : \mathbb{R} \rightarrow \mathbb{R}^{64}$	$v_4 : \mathbb{R} \rightarrow \mathbb{R}^{32}$	2	2	GeLU
Up2	$v_4 : \mathbb{R} \rightarrow \mathbb{R}^{32}$	$v_5 : \mathbb{R} \rightarrow \mathbb{R}^{16}$	4	4	GeLU
Up3	$v_5 : \mathbb{R} \rightarrow \mathbb{R}^{16}$	$v_6 : \mathbb{R} \rightarrow \mathbb{R}^{16}$	8	6	GeLU
Projection	$v_6 : \mathbb{R} \rightarrow \mathbb{R}^{16}$	$v : \mathbb{R} \rightarrow \mathbb{R}$	8	-	-

Table 1: Neural operator structure for quadratic function experiments

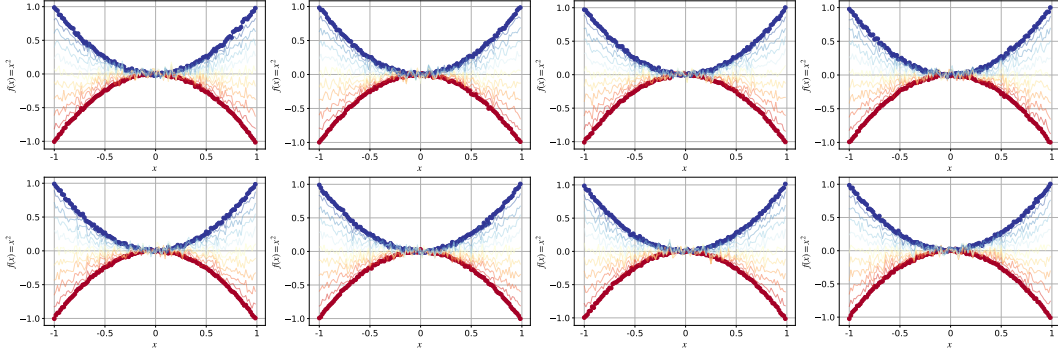


Figure 7: More samples of estimated Brownian bridges between two quadratic functions

$X(0, \cdot) = 0, X(T, \cdot) = s_T - s_0$. Furthermore, we define the unconditional SDE of X as:

$$dX(t) = \int_0^t \tilde{Q}(X(t)) dW(t), \quad X(0) = 0 \quad (33)$$

Where for each shape $s \in H = L^2(\mathbb{R}^d, \mathbb{R}^d)$, $\tilde{Q}(s) : H \rightarrow H$ is a Hilbert-Schmidt operator, defined by some smooth kernel $k \in L^2(\mathbb{R}^d \times \mathbb{R}^d, \mathbb{R}^d)$ as:

$$\tilde{Q}(s)(f(t, \xi)) = \int_{\mathbb{R}^d} k(s(\xi) + \xi, \eta) f(t, \eta) d\eta, \quad \eta \in \mathbb{R}^d \quad (34)$$

The SDE 33 is first defined in [Kunita and Kunita, 1990]. This formulation ensures that the described process is diffeomorphic, which is required for shape evolution since the shape change must be smooth and invertible. In our experiment, we choose the butterfly shapes live in \mathbb{R}^2 , and choose the kernel k to be 2D-Gaussian, i.e., $k(x, y) = \sigma \exp(-\|x - y\|^2 / \kappa)$. Specifically, we set the domain in \mathbb{R}^2 to be finite as $[-0.5, 1.5]^2$ and discretize it with the resolution of 50×50 , we then choose the kernel with $\sigma = 0.04$ and $\kappa = 0.02$, which allows only the correlations within small areas. We then design the operator as Table 3. We train with 20,000 i.i.d. batched samples and with a batch size of 16. We chose the Adam optimizer with an initial learning rate of 0.001 and cosine decay to $1e-5$ as 80% of the training is finished.

The butterfly images are obtained from gbif.org [GBIF.Org User, 2024], and are segmented with the Python package *Segment Anything* [Kirillov et al., 2023] and *Grounding Dino* [Liu et al., 2023b]. The assigned landmarks are interpolated to be evenly distributed along the outlines, then aligned by the R package *Germorph v.4.06* [Adams and Otárola-Castillo, 2013] and normalized into $[0, 1]$ intervals.

Layer	Input	Output	Grid size	Fourier modes	Activation
Lifting	$u : \mathbb{R} \rightarrow \mathbb{R}^2$	$v_0 : \mathbb{R} \rightarrow \mathbb{R}^{16}$	16	-	-
Down1	$v_0 : \mathbb{R} \rightarrow \mathbb{R}^{16}$	$v_1 : \mathbb{R} \rightarrow \mathbb{R}^{16}$	16	8	GeLU
Down2	$v_1 : \mathbb{R} \rightarrow \mathbb{R}^{16}$	$v_2 : \mathbb{R} \rightarrow \mathbb{R}^{32}$	8	6	GeLU
Down3	$v_2 : \mathbb{R} \rightarrow \mathbb{R}^{32}$	$v_3 : \mathbb{R} \rightarrow \mathbb{R}^{64}$	4	4	GeLU
Up1	$v_3 : \mathbb{R} \rightarrow \mathbb{R}^{64}$	$v_4 : \mathbb{R} \rightarrow \mathbb{R}^{32}$	4	4	GeLU
Up2	$v_4 : \mathbb{R} \rightarrow \mathbb{R}^{32}$	$v_5 : \mathbb{R} \rightarrow \mathbb{R}^{16}$	8	6	GeLU
Up3	$v_5 : \mathbb{R} \rightarrow \mathbb{R}^{16}$	$v_6 : \mathbb{R} \rightarrow \mathbb{R}^{16}$	16	8	GeLU
Projection	$v_6 : \mathbb{R} \rightarrow \mathbb{R}^{16}$	$v : \mathbb{R} \rightarrow \mathbb{R}^2$	16	-	-

Table 2: Neural operator structure for circle experiments

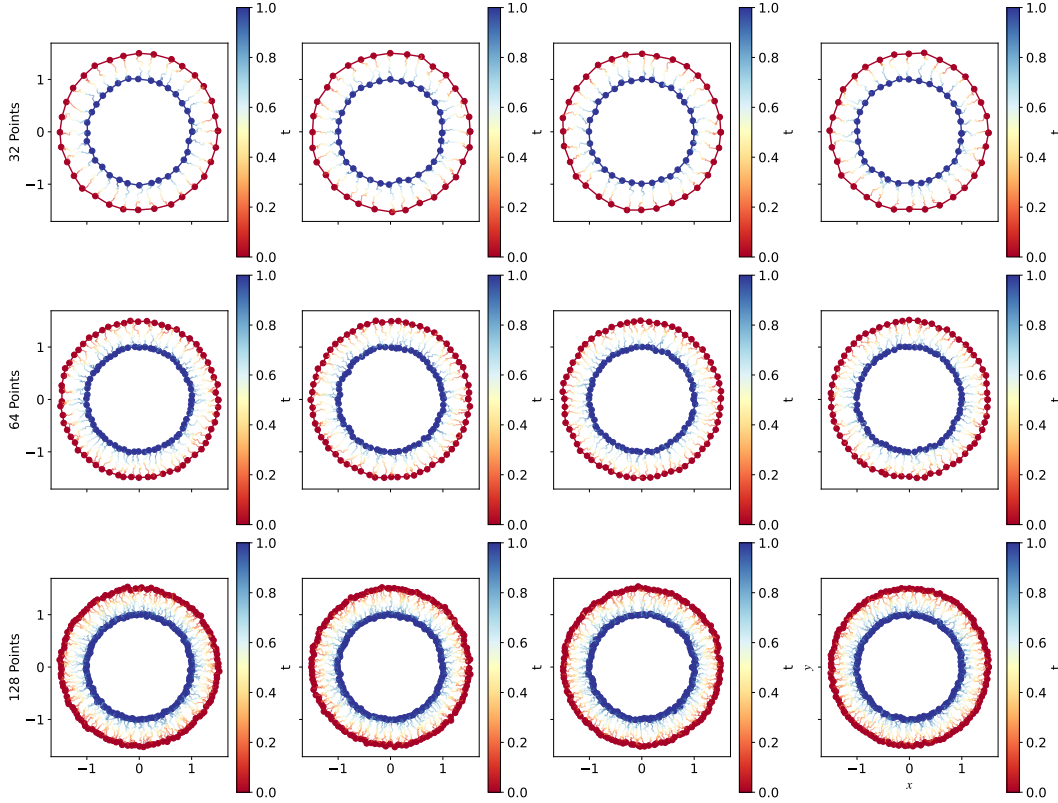


Figure 8: More samples of estimated Brownian bridges between two circles, evaluated under different levels of discretization

Layer	Input	Output	Grid size	Fourier modes	Activation
Lifting	$u : \mathbb{R} \rightarrow \mathbb{R}^2$	$v_0 : \mathbb{R} \rightarrow \mathbb{R}^{16}$	32	-	-
Down1	$v_0 : \mathbb{R} \rightarrow \mathbb{R}^{16}$	$v_1 : \mathbb{R} \rightarrow \mathbb{R}^{16}$	32	16	GeLU
Down2	$v_1 : \mathbb{R} \rightarrow \mathbb{R}^{16}$	$v_2 : \mathbb{R} \rightarrow \mathbb{R}^{32}$	16	8	GeLU
Down3	$v_2 : \mathbb{R} \rightarrow \mathbb{R}^{32}$	$v_3 : \mathbb{R} \rightarrow \mathbb{R}^{64}$	8	6	GeLU
Down4	$v_3 : \mathbb{R} \rightarrow \mathbb{R}^{64}$	$v_4 : \mathbb{R} \rightarrow \mathbb{R}^{64}$	8	6	GeLU
Up1	$v_4 : \mathbb{R} \rightarrow \mathbb{R}^{64}$	$v_5 : \mathbb{R} \rightarrow \mathbb{R}^{64}$	8	6	GeLU
Up2	$v_5 : \mathbb{R} \rightarrow \mathbb{R}^{64}$	$v_6 : \mathbb{R} \rightarrow \mathbb{R}^{32}$	8	6	GeLU
Up3	$v_6 : \mathbb{R} \rightarrow \mathbb{R}^{32}$	$v_7 : \mathbb{R} \rightarrow \mathbb{R}^{16}$	16	8	GeLU
Up4	$v_7 : \mathbb{R} \rightarrow \mathbb{R}^{16}$	$v_8 : \mathbb{R} \rightarrow \mathbb{R}^{16}$	32	16	GeLU
Projection	$v_8 : \mathbb{R} \rightarrow \mathbb{R}^{16}$	$v : \mathbb{R} \rightarrow \mathbb{R}^2$	32	-	-

Table 3: Neural operator structure for butterfly experiments

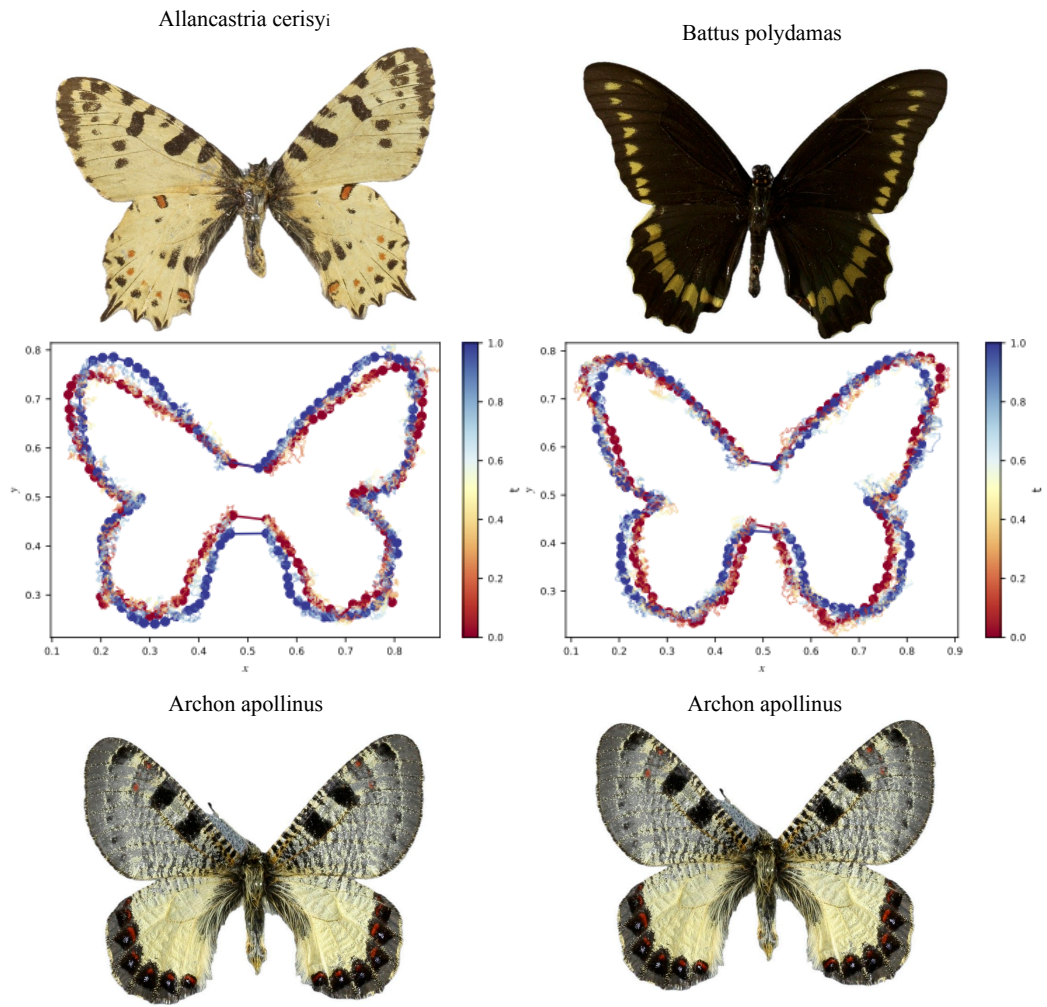


Figure 9: The additional bridge simulations between different species, the bridges are constructed between *Archon apollinus* (blue) and *Allancastris cerisyi*/*Battus polydamas* (red).

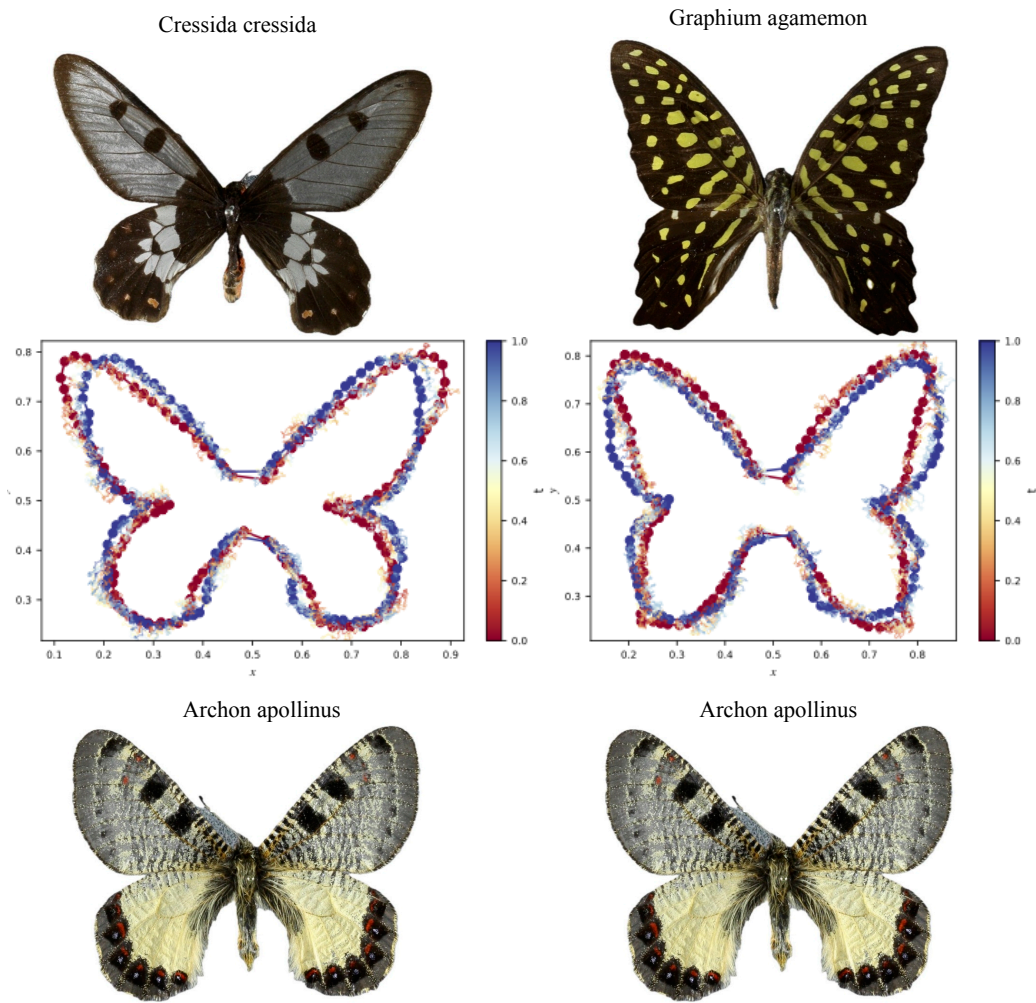


Figure 10: The additional bridge simulations between different species, the bridges are constructed between *Archon apollinus* (blue) and *Cressida cressida*/*Graphium agamemon* (red).